RSC Advances

ROYAL SOCIETY OF CHEMISTRY

www.rsc.org/advances

Cite this: DOI: 10.1039/c0xx00000x

www.rsc.org/xxxxxx

ARTICLE TYPE

Reduced Graphene Oxide Anchored Magnetic $ZnFe_2O_4$ Nanoparticles with Enhanced Visible Light Photocatalytic Activity

Shouliang Wu, Panpan Wang, Yunyu Cai, Dewei Liang, Yixing Ye, Zhenfei Tian, Jun Liu and Changhao Liang*

Received (in XXX, XXX) Xth XXXXXXXXX 20XX, Accepted Xth XXXXXXXXX 20XX
DOI: 10.1039/b000000x

We report a facile approach to immobilize magnetic $ZnFe_2O_4$ nanoparticles (NPs) onto reduced grapheme oxide (rGO) network by using highly reactive $ZnO_x(OH)_y$ and FeO_x colloids as precursors, which were respectively obtained by laser ablation of metallic zinc (Zn) and iron (Fe) target in pure water. Microstructure investigation of such nanocomposites (NCs) revealed that $ZnFe_2O_4$ NPs are well-dispersed onto rGO sheets. Such structure was helpful for separating the photoexcited electron-hole pairs and accelerating the electrons transfer. Electrochemical impedance measurements indicated the remarkably decrease of interfacial layer resistance of composite structure in compared to that of pure $ZnFe_2O_4$ NPs. As a result of these advantages, such NCs present a prominent enhancement in photodegradation efficiency of methylene blue dye. Besides, the excellent magnetic properties of $ZnFe_2O_4$ NPs allow the catalysts being easily separated from the solution by a magnet for recycle utilization. This effort not only provided a new approach to fabricate $ZnFe_2O_4$-rGO NCs, also expanded the application of $ZnFe_2O_4$ NPs used as a visible-light excited photocatalysts in application of organic pollutants degradation.

Introduction

Semiconductor composited with grapheme could be a critical approach to improve its photoelectric properties due to the outstanding characteristics of graphene, such as prominent thermal stability, superior electronic conductivity, remarkable structural flexibility, high specific surface area and low manufacturing expense.[1-6] Transition-metal oxides such as Fe_2O_3, CoO, Mn_3O_4 were loaded onto graphene as anode materials for lithium-ion batteries.[7-12] These nanohybrids exhibit higher reversible capacities, much more excellent recyclability and better cell stability in comparison to their bare counterparts. Co_3O_4 NPs composited graphene presented high sensitivity in probing glucose in a micro-droplet as a non-enzymatic sensor.[13,14] Furthermore, semiconductor photocatalysts such as TiO_2, ZnO, SnO_2 incorporated into graphene show capabilities to extend the light absorption range, increase the absorptive capacity of pollutants, and contribute to the charge carrier separation and transmission.[15-19]

Zinc ferrite ($ZnFe_2O_4$) is one of the iron-based cubic spinel series showing advantages of a narrow band gap (1.92 eV) for high absorption efficiency of sunlight, high photochemical stability, low cost and excellent ferromagnetic properties for magnetic separation from suspensions.[20-23] However, individual $ZnFe_2O_4$ nanomaterials are rarely utilized as a photocatalyst in the degradation of pollutants owing to the notable drawbacks. That is, the $ZnFe_2O_4$ NPs are tending to aggregate due to the ferromagnetic property under room temperature, the narrow band-gap results in the rapid recombination of photo-induced carriers. Two-dimensional honeycomb structure of graphene is appropriate as a supporting substrate to hinder the aggregation of $ZnFe_2O_4$ NPs, while its superior electrical conductivity, satisfy the quick transfer of electrons and avoid the recombination of photo-induced electron-hole pairs. Therefore, well-dispersed the $ZnFe_2O_4$ NPs onto graphene network could be an effective route to improve its photocatalytic performance.

In this study, we present an alternative approach to anchor $ZnFe_2O_4$ NPs onto graphene substrate through a combination utilization of laser ablation in liquids (LAL) technique and hydrothermal treatment. LAL of Zn and Fe target can induce the formation of highly reactive colloidal NPs without using of any organic surfactants. In subsequent assembly and growth processes of colloidal NPs, the resulted $ZnFe_2O_4$ NPs can be uniformly anchored onto rGO network. In comparison with the pure $ZnFe_2O_4$ NPs, the $ZnFe_2O_4$-rGO NCs presented higher photocatalytic activity in degradation of methylene blue (MB) under visible-light irradiation.

Experimental

2.1. Materials preparation

The synthesis process of the nanocomposite was shown in Scheme 1. First, a Fe (99.99%) or Zn (99.99%) target was installed in the bottom of a vessel filled with 15 mL deionized water. The Fe target was ablated for 30 min and Zn target for 15 min, respectively, by using a fundamental (1064 nm) Nd:YAG pulse laser with a 10 Hz pulse repetition rate, 10 ns pulse duration, and 100 mJ pulse energy density. Second, the obtained $ZnO_x(OH)_y$ colloids was mixed with 3 mL ammonia solution (25-

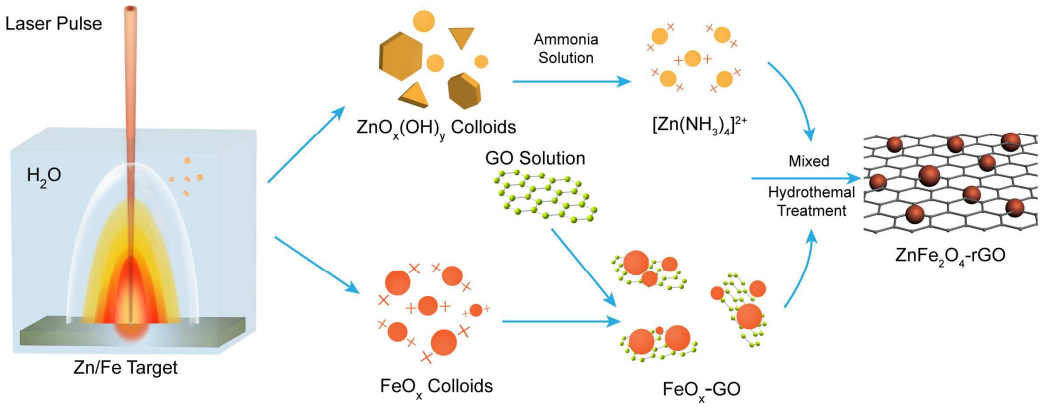

Scheme 1 Illustration for the synthesis of $ZnFe_2O_4$-rGO NCs.

28 wt.%) and the colloidal solution gradually became transparent. On the other hand, LAL generated FeO_x colloids was mixed with 5 mL graphene oxide (GO) solution under magnetic stirring for 30 min. Afterwards, the above separately treated $ZnO_x(OH)_y$ and FeO_x colloidal solutions were put into a 50 mL autoclave and then hydrothermally treated at 180°C for 12 h. The product was collected by a magnet, washed with deionized water and anhydrous ethanol alternately, and then dried in a vacuum-dry box at 60°C for 6 h.

The preparation procedures of pure $ZnFe_2O_4$ NPs are similar to the above elucidation for the preparation of the $ZnFe_2O_4$-rGO NCs, except for without addition of GO suspension. The GO used in the present experiments was synthesized from natural graphite by using the modified Hummers method.[24, 25]

2.2. Characterization

The phase structure of the obtained products were analyzed by a Rigaku X-ray diffract meter with Cu Kα radiation (λ = 0.15419 nm). Surface chemical constituents of the products were monitored by X-ray photoelectron spectroscopy (XPS, Thermo ESCACLB 250). The Raman spectra were collected by a confocal microprobe Raman (RENISHAW in Via Raman Microscope) with a 532 nm Argon ion laser excitation. A transmission electron microscopy (TEM) (JEOL, JEM-2010) with 200 kV acceleration voltages was used to investigate the morphology and structure of the composite. TEM specimen was made by dispersing the product powders in ethanol to form a suspension which was then dropped onto a carbon-coated Cu grid after ultrasonic treatment. Electrochemical impedance spectroscopy (EIS) analysis of the products was made using a Zahner IM6e electrochemical workstation. Magnetic property measurement was carried out using a superconducting quantum interference device magnetometer (SQUID, Quantum Design MPMS) under an applied field in the range of -10000 Oe to 10000 Oe at 300 K.

2.3. Photocatalytic activity evaluation

The photocatalytic activity of the NCs was evaluated for the degradation of MB under visible light irradiation. Prior to irradiation, 3 mg photocatalysts were mixed with 35 mL 12 ppm MB solution in a 50 mL test tube and sonicated for 10 min. Afterwards, the mixture was magnetically stirred in the dark for 2 h to reach the complete absorption-desorption equilibrium, 0.6 mL hydrogen peroxide solution (H_2O_2, 30 w.t.%) was subsequently added. The mixture was subsequently illuminated by a 500W xenon lamp with a distance of 40 cm. A wave filter plate ($\lambda > 420$ nm) was used to completely remove any irradiation below 420 nm. At different time intervals, about 4 mL mixed solution was sampled and all the photocatalysts were magnetically separated by a magnet in a dark environment. The concentration of the remained MB was analyzed by measuring the absorption intensity at featured wavelength of 664 nm. One of the test tubes has been compared without any photocatalysts used but only 0.6 mL H_2O_2 for blank experiments.

Results and discussion

To investigate the morphology and structure of the products, structural characterizations were taken for the $ZnFe_2O_4$-rGO NCs and pure $ZnFe_2O_4$ NPs. TEM image in Figure 1a indicates that large quantities of $ZnFe_2O_4$ NPs are dispersed on rGO nanosheets. The high-resolution TEM (HRTEM) image of $ZnFe_2O_4$ NPs (the upper right inset of Figure 1a) give the crystalline lattice fringes with *d*-spacing of 0.489 nm and 0.299 nm, which can be assigned to the (111) and (220) planes of the cubic-structured $ZnFe_2O_4$. These results are well consistent with the XRD analysis that presented in Figure 2a. Moreover, it worth noting that, even after a long time of sonication, the $ZnFe_2O_4$ NPs are still firmly anchored on the surface of rGO sheets uniformly, suggesting the strong interaction between the $ZnFe_2O_4$ NPs and the rGO sheets. However, without the presence of rGO sheets, the prepared pure $ZnFe_2O_4$ NPs aggregate into large particles (see Figure 1b). XRD pattern of pure $ZnFe_2O_4$ NPs was shown in Figure S1. Therefore, the rGO sheets play an important role in preventing the agglomeration of $ZnFe_2O_4$ NPs, and conversely the well-dispersed $ZnFe_2O_4$ NPs also prevent the overlapping of rGO sheets.

Figure 2a shows the XRD pattern of $ZnFe_2O_4$-rGO NCs. Evidently, all the diffraction peaks can be assigned to cubic $ZnFe_2O_4$ in a spinel structure (JCPDS NO. 82-1042), and no characteristic peaks of impurities are detected. The diffraction peaks at 2θ values of 29.9º, 35.2º, 42.8º, 53.0º, 56.6º and 62.1º can be attributed to the reflection of (220), (311), (400), (422), (511) and (440) planes, respectively. However, there is no obvious diffraction peak of rGO which has a broad peak at around 23-27°,[26-28] suggesting that the rGO sheets were

exfoliated by decorating $ZnFe_2O_4$ NPs during the hydrothermal

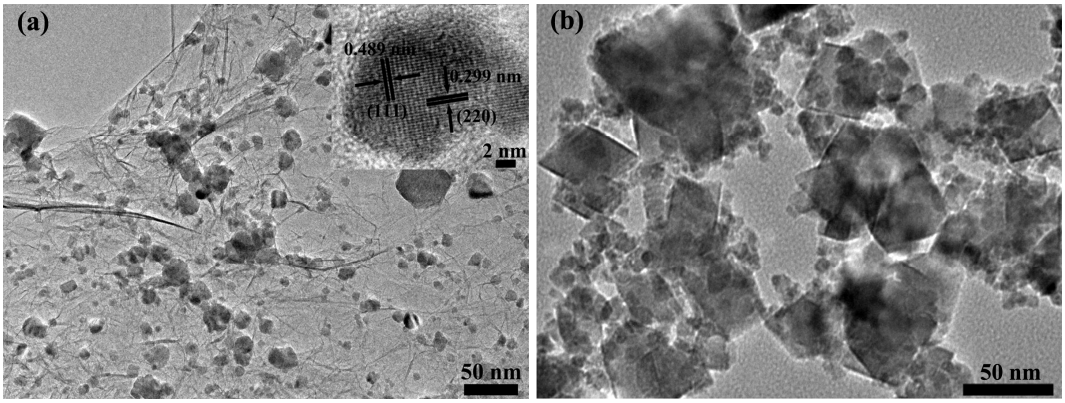

Figure 1. TEM and HRTEM images of $ZnFe_2O_4$-rGO NCs (a) and pure $ZnFe_2O_4$ NPs (b).

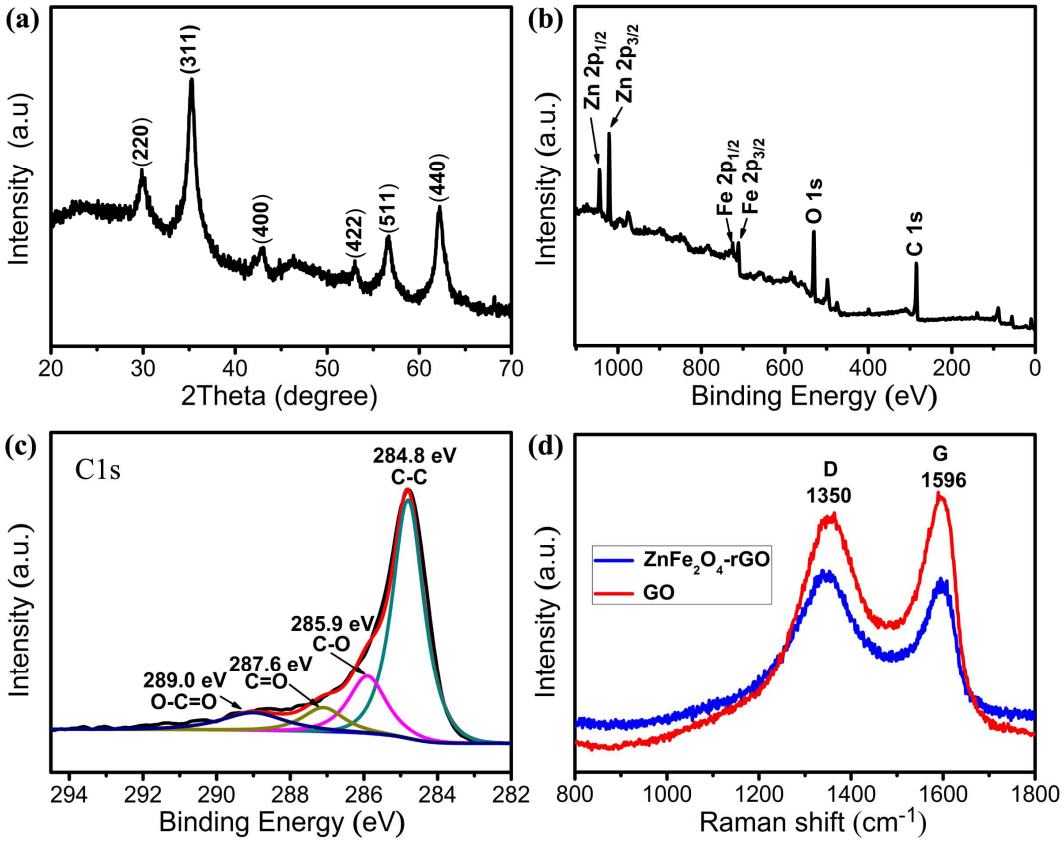

Figure 2. (a) XRD pattern of $ZnFe_2O_4$-rGO NCs. Overall (b) and high-resolution C1s (c) XPS spectrum of $ZnFe_2O_4$-rGO NCs. (d) Raman spectra of GO and $ZnFe_2O_4$-rGO NCs.

reaction.[28,29] Important information on the surface electronic state and the composition of the final products can be further provided by XPS. As shown in Figure 2b, the overall XPS spectrum demonstrated that the obtained products contain elements of Zn, Fe, O and C. According to the high-resolution Zn2p (Figure S2a) and Fe2p (Figure S2b) XPS spectrum, the Zn and Fe exist as Zn^{2+} and Fe^{3+}oxidation states, respectively.[22,30] The high-resolution C1s XPS spectrum (Figure 2c) can be divided into four peaks corresponding to carbon atoms in different oxygen-containing functional groups. The peak located at binding energy of 284.8 eV is assigned to C−C bond, which present the highest intensity. However, other three peaks located at binding energy of 285.9, 287.6 and 289.0 eV are corresponding to the C−O, C=O and O−C=O bond, which show much weaker intensity. By comparison with high-resolution XPS spectrum of C1s in GO (Figure S3), it inferred that GO has been reduced into rGO sheets after hydrothermal reactions.[31] Raman spectra (Figure 2d) of GO and $ZnFe_2O_4$-rGO NCs both show two characteristic peaks at about 1350 cm^{-1} (D band) and 1596 cm^{-1} (G band). However, the intensity ratio ($r = I_D/I_G$) for $ZnFe_2O_4$-rGO NCs (r = 1.07) displayed a larger value compared with that of GO (r = 0.91), which further demonstrated that the GO has been deoxygenated

and reduced into rGO.[32,33] Totally, above investigations revealed that both of the reduction of GO and loading of the $ZnFe_2O_4$ NPs were achieved during the hydrothermal reaction.

Also, the formation mechanism of $ZnFe_2O_4$-rGO NCs was proposed as following. In our previous work, we have confirmed that the fresh colloids produced by LAL of a Zn target in pure water were mainly composed of ZnO, $Zn(OH)_2$ and a small amount of Zn NPs using similar laser parameters, therefore, the sample can be nominally described as $ZnO_x(OH)_y$.[34] In this experiments, when the ammonia was added, the $ZnO_x(OH)_y$ colloids can react with NH_4^+ to generate $Zn(NH_3)_4^{2+}$ as below equation:

$$ZnO_x(OH)_y + NH_4^+ \rightarrow Zn(NH_3)_4^{2+} + H_2O \quad (1)$$

In addition, according to XRD pattern (Figure S4) of the fresh colloids obtained by LAL of a Fe target in pure water, it was found that the colloids were mainly composed of FeO, as described as FeO_x. The fresh LAL-derived FeO_x colloidal solution shows a positive ξ potential of + 21.7 mV measured by a MALVERN instrument (Zetasizer3000HSa). When the fresh electropositive FeO_x colloids were added into the GO solution, owing to the electronegative groups such as hydroxyl, carboxyl or epoxy groups on the edges of GO sheets, the FeO_x colloids would be easily captured by the electrostatic force. According to the TEM image of the FeO_x-GO NCs (Figure S5), the FeO_x NPs were well dispersed on the GO sheets. When these treated $ZnO_x(OH)_y$ and FeO_x colloidal solution was mixed, $Zn(NH_3)_4^{2+}$ would react with the FeO_x NPs on the surface of GO sheets under the 180°C hydrothermal treatment, simultaneously GO was reduced into rGO. The above reaction can be represented by the following equation:

$$Zn(NH_3)_4^{2+} + FeO_x + OH^- \rightarrow ZnFe_2O_4 + NH_3 + H_2O \quad (2)$$

Through a series of contrast tests (see Figure S6), we have proved that pure $ZnFe_2O_4$ can only be obtained at suitable amount of added ammonia (3 mL). Excessive or insufficient amount of ammonia was both not benefit for the formation of pure $ZnFe_2O_4$. Besides, by hydrothermal treating of two other LAL-induced highly reactive colloids, this synthetic strategy was universal to prepare many other different kinds of pure ternary compounds, some of which as showing in Figure S7.

Figure 3 shows the typical EIS spectra of pure $ZnFe_2O_4$ NPs and $ZnFe_2O_4$-rGO NCs as Nyquist plots. It is observed that, with the introduction of the rGO sheets, the semicircle in the plot became shorter, indicating a decrease in the solid state interfacial layer resistance and the charge transfer resistance on the surface,[2,35] also a good connection between the $ZnFe_2O_4$ NPs and rGO sheets. Considering the excellent electron collection and transfer properties of the $ZnFe_2O_4$-rGO NCs, we supported the suggestion of using as prepared NCs for photocatalytic application.

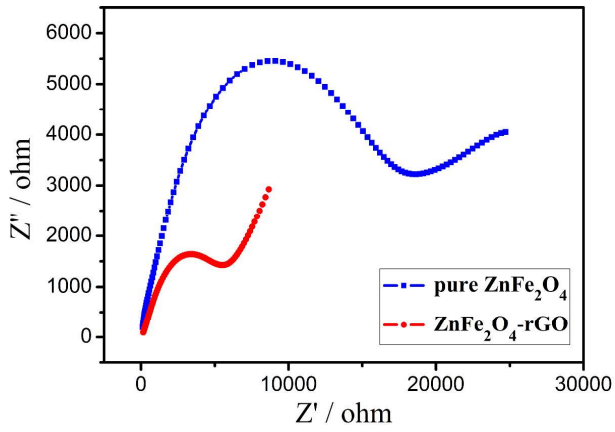

Figure 3. EIS spectra of pure $ZnFe_2O_4$ NPs (blue) and $ZnFe_2O_4$-rGO NCs (red).

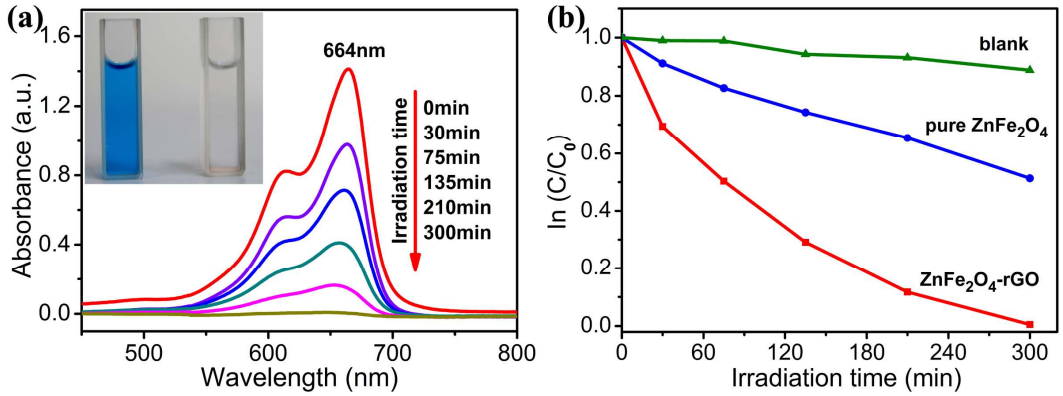

Figure 4. (a) Representative evolution of absorption of 12 ppm MB degraded by 3 mg $ZnFe_2O_4$-rGO NCs under visible-light irradiation in the presence of H_2O_2. Upper left inset is the optic image of 12 ppm MB solution before and after degradation. (b) Degradation curves of MB under different situations: 0.6 mL H_2O_2 and without any catalysts (green), pure $ZnFe_2O_4$ NPs + 0.6 mL H_2O_2 (blue), $ZnFe_2O_4$-rGO NCs + 0.6 mL H_2O_2 (red).

The photocatalytic activity of the as-prepared products was evaluated for MB degradation under visible-light irradiation. Figure 4 shows the degradation behaviors of MB under different situations. The absorption-desorption equilibrium MB solution was used as the starting solution and its peak value at 664 nm was used to monitor the degradation rate. Figure 4a displays the changes in the optical absorption spectra of MB in the presence of $ZnFe_2O_4$-rGO NCs and H_2O_2 under visible-light (λ > 420 nm).

After 300 min, the absorption peak at 664 nm disappeared and the solution became transparent (upper left inset in Figure 4a), indicated that the MB has been degraded completely within 300 min. The degradation rates of the MB solution by using different photocatalysts were calculated as shown in Figure 4b. First, as a blank contrast, when the MB solution was only added with H_2O_2, the absorption peak at 664 nm is nearly unchanged after irradiation for 300 min. Subsequently, when the pure $ZnFe_2O_4$

NPs were used as photocatalysts, the photodegradation rate reached to nearly 50% after 300 min. However, the degradation rate of the MB sharply increased to 99.5% when using the $ZnFe_2O_4$-rGO NCs as the photocatalysts.

Scheme 2 depicts the sketches of the basic structure of the $ZnFe_2O_4$-rGO NCs and the electron-transfer processes between $ZnFe_2O_4$ NPs and the rGO sheets after being activated by the visible-light ($\lambda > 420$ nm). The photo-excited electrons migrated from the valence band of $ZnFe_2O_4$ NPs to the conduction band, leaving the holes in the valence band. However, this photo-excited electron-hole pairs are unstable and can easily recombine, which results in low efficiency of photocatalyst. When the $ZnFe_2O_4$ NPs were combined with rGO sheets, considering the strong interaction between them, the excited electrons in the conduction band can quickly transfer to the rGO sheets, where they diffuse into trap states. These long-lived trapped electrons can activate the hydrogen peroxide to produce strong oxidant hydroxyl radicals (·OH), which is the main factor for the degradation of MB.[28,36]

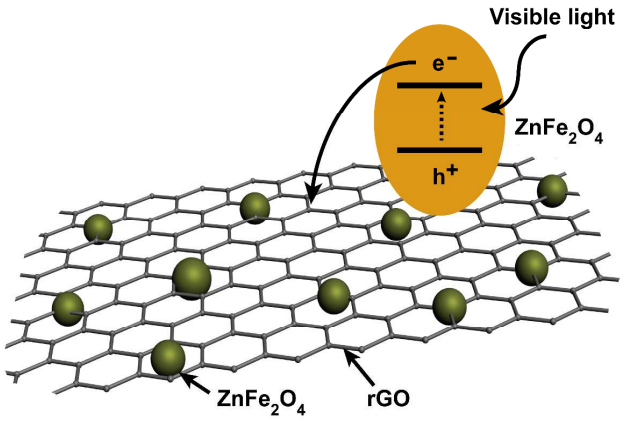

Scheme 2 Electron transfer process in the $ZnFe_2O_4$-rGO NCs.

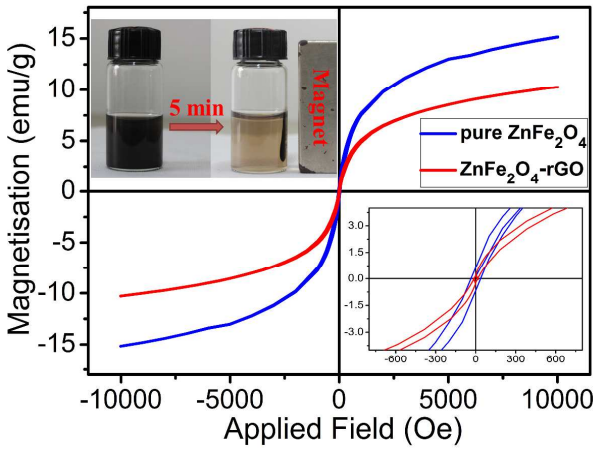

Figure 5. Room-temperature magnetic hysteresis loops for pure $ZnFe_2O_4$ NPs (blue) and $ZnFe_2O_4$-rGO NCs (red). The inset located at lower right corner shows a magnification of the loops in the range of −800 to 800 Oe. The inset located at upper left corner display the photographs of $ZnFe_2O_4$-rGO NCs separated by an external magnet from the aqueous solution.

Figure 5 display the magnetic hysteresis loops of the pure $ZnFe_2O_4$ NPs (blue line) and $ZnFe_2O_4$-rGO NCs (red line). Both of them exhibit a ferromagnetic behavior at room temperature, and their magnetic saturation (Ms) values are 15.2 and 10.3 emu/g, respectively. The magnetic separation properties of the obtained $ZnFe_2O_4$-rGO NCs were tested in water by placing a magnet near the glass bottle (upper left inset). The most photocatalysts can be quickly separated from the solution by the attraction of the magnet within 5 min. This result not only further confirmed the excellent contacted between pure $ZnFe_2O_4$ NPs with rGO sheets, but also make this composite a promising candidate for recycle utilization as photocatalyst.

Conclusions

In summary, we reported the utilization of LAL-induced $ZnO_x(OH)_y$ and FeO_x colloids as chemical-friendly reactive precursors to grow $ZnFe_2O_4$-rGO NCs as visible-light photocatalyst. Magnetic $ZnFe_2O_4$ NPs were immobilized onto simultaneously reduced grapheme oxide (rGO) network. The photocatalytic activity of $ZnFe_2O_4$-rGO NCs was obviously enhanced in compared with that of pure $ZnFe_2O_4$ NPs, due to the effective restraint of the recombination of the photo-excited electron-hole pairs by rGO sheets and the generation of strong oxidant radical ·OH. Together considering the magnetic separation ability and stability, $ZnFe_2O_4$-rGO NCs show promising as a candidate visible-light photocatalyst for repeatedly organic pollutants degradation.

Acknowledgements

This work was financially supported by the National Basic Research Program of China (2014CB931704), the National Natural Science Foundation of China (NSFC, No. 11304315, 51401206, 11204308), the CAS/SAFEA International Partnership Program for Creative Research Teams and the Instrument Developing Project of the Chinese Academy of Sciences under Grant No. YG2012065.

Notes and references

Key Laboratory of Materials Physics and Anhui Key Laboratory of Nanomaterials and Nanotechnology, Institute of Solid State Physics, Hefei Institutes of Physical Science, Chinese Academy of Sciences, Hefei, 230031, PR China. Fax: 86-551-65591434; Tel: 86-551-65591129; E-mail: chliang@issp.ac.cn;

†Electronic Supplementary Information (ESI) available: XPS spectrum of Zn2p (a) and Fe2p (b) from $ZnFe_2O_4$-rGO NCs, XPS spectrum of C1s from GO, XRD pattern of the fresh FeO_x colloidal NPs, and TEM image of FeO_x-GO NCs.

1 Q. J. Xiang, J. G. Yu, M. Jaroniec, *Chem. Soc. Rev.*, 2012, **41,** 782.
2 H. Zhang, X. J. Lv, Y. M. Li, Y. Wang, J. H. Li, *ACS Nano*, 2010, **4**, 380.
3 E. P. Gao, W. Z. Wang, M. Shang, J. H. Xu, *Phys. Chem. Chem. Phys.*, 2011, **13**, 2887.
4 G. H. Yu, L. B. Hu, M. Vosgueritchian, H. L. Wang, X. Xie, J. R. McDonough, X. Cui, Y. Cui, Z. N. Bao, *Nano Lett.*, 2011, **11**, 2905.
5 Y. X. Ye, P. P. Wang, E. M. Dai, J. Liu, Z. F. Tian, C. H. Liang, G. S. Shao, *Phys. Chem. Chem. Phys.*, 2014, **16**, 8801.
6 S. Z. Deng, V. Tjoa, H. M. Fan, H. R. Tan, D. Sayle, M. Olivo, S. Mhaisalkar, J. Wei, C. H. Sow, *J. Am. Chem. Soc.*, 2012, **134**, 4905.
7 X. J. Zhu, Y. W. Zhu, S. Murali, M. D. Stoller, R. S. Ruoff, *ACS Nano*, 2011, **5**, 3333.
8 M. Zhang, B. H. Qu, D. N. Lei, Y. J. Chen, X. Z. Yu, L. B. Chen, Q. H. Li, Y. G. Wang, T. H. Wang, *J. Mater. Chem.*, 2012, **22,** 3868.
9 G. M. Zhou, D. W. Wang, F. Li, L. L. Zhang, N. Li, Z. S. Wu, L. Wen, G. Q. Lu, H. M. Cheng, *Chem. Mater.*, 2010, **22,** 5306.

10 Y. M. Sun, X. L. Hu, W. Luo, Y. H. Huang, *J. Phys. Chem. C*, 2012, **116**, 20794.

11 K. J. Zhang, P. X. Han, L. Gu, L. X. Zhang, Z. H. Liu, Q. S. Kong, C. J. Zhang, S. M. Dong, Z. Y. Zhang, J. H. Yao, H. X. Xu, G. L. Cui, L. Q. Chen, *ACS Appl. Mater. Interfaces*, 2012, **4,** 658.

12 H. L. Wang, L. F Cui, Y. Yang, H. S. Casalongue, J. T. Robinson, Y. Y. Liang, Y. Cui, H. J. Dai, *J. Am. Chem. Soc.*, 2010, **132**, 13978.

13 X. W. Wang, X. C. Dong, Y. Q. Wen, C. M. Li, Q. H. Xiong, P. Chen, *Chem. Commun.*, 2012, **48**, 6490.

14 X. C. Dong, H. X. Xu, X. W. Wang, Y. X. Huang, M. B. Chan-Park, H. Zhang, L. H. Wang, W. Huang, P. Chen, *ACS Nano*, 2012, **6**, 3206.

15 Y. S. Fu, X. Q. Sun, X. Wang, *Materials Chemistry and Physics*, 2011, **131,** 325.

16 Y. H. Zhang, Z. R. Tang, X. Z. Fu, Y. J. Xu, *Acs Nano*, 2010, **4**, 7303.

17 B. J. Li, H. Q. Cao, *J. Mater. Chem.*, 2011, **21**, 3346.

18 H. Seema, K. C. Kemp, V. Chandra, K. S. Kim, *Nanotechnology*, 2012, **23**, 355705.

19 X. Q. An, J. C. Yu, Y. Wang, Y. M. Hu, X. L. Yu, G. J. Zhang, *J. Mater. Chem.*, 2012, **22,** 8525.

20 Y. J. Yao, J. C. Qin, Y. M. Cai, F. Y. Wei, F. Lu, S. B. Wang, *Environ Sci Pollut Res*, 2014, **21,** 7296.

21 Z. H. Yuan, L. D. Zhang, *J. Mater. Chem.*, 2011, **11**, 1265.

22 H. J. Lv, L. Ma, P. Zeng, D. N. Ke, T. Y. Peng, *J. Mater. Chem.*, 2010, **20**, 3665.

23 P. P. Hankare, R. P. Patil, A. V. Jadhav, K. M. Garadkar, R. Sasikala, *Applied Catalysis B: Environmental*, 2011, **107**, 333.

24 W. S. Hummers, Jr., R. E. Offeman, *J. Am. Chem. Soc.*, 1958, **80,** 1339.

25 Y. X. Xu, H. Bai, G. W. Lu, C. Li, G. Q. Shi, *J. Am. Chem. Soc.*, 2008, **130,** 5856.

26 J. Su, M. H. Cao, L. Ren, C. W. Hu, *J. Phys. Chem. C*, 2011, **115**, 14469.

27 J. Z. Wang, C. Zhong, D. Wexler, N. H. Idris, Z. X. Wang, L. Q. Chen, H. K. Liu, *Chem. Eur. J.*, 2011, **17**, 661.

28 Y. S. Fu, X. Wang, *Ind. Eng. Chem. Res.*, 2011, **50**, 7210.

29 C. Xu, X. Wang, J. Zhu, *J. Phys. Chem. C*, 2008, **112**, 19841.

30 Y. Hou, X. Y. Li, Q. D. Zhao, X. Quan, G. H. Chen, *Adv. Funct. Mater.*, 2010, **20**, 2165.

31 Y. M. Sun, X. L. Hu, W. Luo, Y. H. Huang, *ACS Nano*, 2011, **5,** 7100.

32 X. Y. Li, X. L. Huang, D. P. Liu, X. Wang, S. Y. Song, L. Zhou, H. J. Zhang, *J. Phys. Chem. C*, 2011, **115**, 21567.

33 Z. Y. Ji, X. P. Shen, G. X. Zhu, K. M. Chen, G. H. Fu, L. Tong, *Journal of Electroanalytical Chemistry*, 2012, **682,** 95.

34 Z. F. Tian, C. H. Liang, J. Liu, H. M. Zhang, L. D. Zhang, *J. Mater. Chem.*, 2012, **22,** 17210.

35 Y. Y. Cai, P. P. Wang, Y. X. Ye, J. Liu, Z. F. Tian, Y. S. Liu, C. H. Liang, *RSC Adv.*, 2013, **3**, 19064.

36 D. B. Lu, Y. Zhang, S. X. Lin, L. T. Wang, C. M. Wang, *Journal of Alloys and Compounds*, 2013, **579**, 336.

Graphic abstract

Title: Reduced graphene oxide anchored magnetic $ZnFe_2O_4$ nanoparticles with enhanced visible-light photocatalytic activity

Author: Shouliang Wu, Panpan Wang, Yunyu Cai, Dewei Liang, Yixing Ye, Zhenfei Tian, Jun Liu and Changhao Liang*

A colloidal approach was developed to immobilize magnetic $ZnFe_2O_4$ onto simultaneously reduced GO toward degradation of dyes under visible-light irradiation.

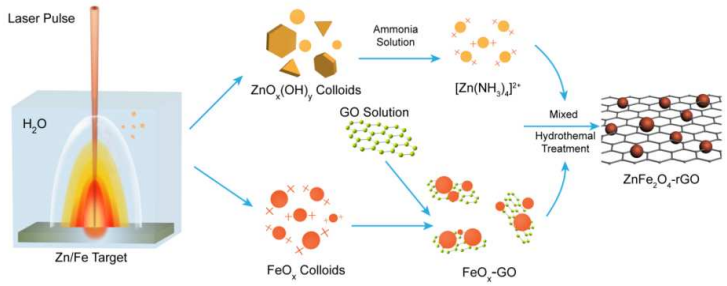

Figure for TOC